Hindawi
Shock and Vibration
Volume 2021, Article ID 8976731, 14 pages
https://doi.org/10.1155/2021/8976731

Research Article

Numerical Investigation on Vibration Performance of an Improved Switched Reluctance Machine with Double Auxiliary Slots

Zhengyuan Gao, Shanming Wang, Zhiguo An, and Pengfei Sun

School of Mechatronics and Vehicle Engineering, Chongqing Jiaotong University, Chongqing 400074, China

Correspondence should be addressed to Zhiguo An; anzhiguo@cqjtu.edu.cn and Pengfei Sun; danny25@163.com

Received 19 May 2021; Accepted 26 October 2021; Published 24 November 2021

Academic Editor: Francesco Bucchi

Considerable vibration and acoustic noise limit the further application of Switched Reluctance Machine (SRM) due to its structural characteristics and working principle. An improved SRM model with double auxiliary slots (DAS) was proposed, in which the direction of the magnetic line of force was adjusted, and the radial magnetic density in the air gap was reduced by changing the local tooth profiles of the stator and the rotor. The effects of initial rotor position and turn-on angle and turn-off angle on radial Electromagnetic Force (EMF) and maximum torque were investigated. The results indicate the radial EMF and torque increase significantly with the advancement of the turn-on angle or the delay of the turn-off angle. In the orthogonal experimental design, initial rotor position, turn-on angle, and turn-off angle were taken as the factors, and the optimal set of parameters that minimized radial EMF was determined according to a greater output torque. In contrast to conventional SRM, the radial EMF of the SRM with DAS significantly reduces when the optimal set is applied.

1. Introduction

The switched reluctance machine (SRM) is a variable reluctance machine with double salient poles. It has stator and rotor laminated by silicon steel sheets and windings only on the stator. SRM has the advantages of simple structure, low cost, strong robustness, high operation temperature, small starting current, and large torque [1, 2]. However, its significant structural difference from other electric machines leads to some shortcomings, such as high torque ripple, considerable vibration, and acoustic noise, to limit the wide applications [3–6].

The increasing popularity of SRM has urged researchers and engineers to develop some effective methods to suppress torque ripple, vibration, and acoustic noise of SRM through two ways. On the one hand, the optimization of machine structure was carried out to reduce the radial EMF and weaken the vibration by adjusting structural form and size that affect the vibration characteristics. In the aspect of optimization on the stator structure, Kotegawa and Miki [7] proposed an innovative stator structure to effectively reduce the deformation and vibration and revealed the relationship between the sound pressure level and the maximum displacement of the stator. Davarpanah and Faiz [8] established a novel stator structure with c-type core, which not only can effectively reduce the core loss because of the shortest main magnetic flux path at the stator teeth, but also generate positive torque on two teeth on the same stator phase, as the rotor rotates from the misaligned position to the aligned position. The results show that the average torque of the proposed SRM structure is 17.19% higher than that of the traditional SRM, and the torque ripple is 49.54% lower than that of the traditional SRM. In contrast to the conventional SRM, Isfahani and Fahimi [9] found that the double-stator SRM significantly reduced the radial EMF and vibration. Gupta et al. [10] discussed several design methods to improve the radial magnetic flux of single-tooth winding for double-stator SRM to solve the problem of the high torque

density and large torque ripple and optimized the rotor structure by adjusting the angle along the rotation direction in alternate rotor segments. The simulation results show that the proposed structure improves the torque capacity and suppresses torque ripple in the commutation region. Yu et al. [11] proposed the stator skewed teeth structure and optimized the skew angle to effectively reduce the acoustic noise and vibration. In the aspect of optimization of the rotor structure, Li et al. [12] reduced the torque ripple and the machine vibration by punching hole in the rotor pole and investigated the effects of depth, width, and position of punching hole on the average torque and torque ripple. Zhang et al. [13] verified the effective reduction of the radial EMF and vibration for the rotor skewed teeth structure.

Recently, some achievements on comprehensive consideration of the structural improvement of stator and rotor to reduce the radial EMF were published. The skewed teeth structures of stator and rotor effectively suppress electromagnetic noise and vibration in [14, 15]. Sakuma et al. [16] proposed an improved SRM structure with hexagonal stator yokes, trapezoidal stator teeth, and rotor poles with V-shaped magnetic barrier structures. It is found that the structures of stator and rotor effectively reduce vibration deformation and the radial EMF, respectively. Elamin et al. [17] investigated the effects of rectangular windows on the stator and rotor to suppress acoustic noise and vibration and determined the optimal position, length, and width of the rectangular windows. Takayama and Miki [18] studied the rotor pole with both cutting sides to reduce the maximum radial EMF and acoustic noise and used the hexagonal stator structure with the tapered pole to reduce the stator displacement. Kondelaji and Mirsalim [19] proposed a novel modular SRM using a pole combination mode, which has dual stators and segmented rotors. Comparing five different types of SRMs, the advantages in magnetic linkage and torque of the SRM were illustrated.

On the other hand, many optimal control strategies have been developed to further reduce the radial EMF. Tanabe and Akatsu [20] considered the relationship between the input voltage and vibration acceleration and proposed a low vibration and noise driving method to control a smooth transition during commutation. The results indicate that the method is effective on reduction of the fundamental frequency vibration. Malekipour et al. [21] found that, comparing three different methods of boost voltage in demagnetization, the combination of control algorithms with conventional methods based on asymmetric H-bridge converters can minimize stator vibration. Various current curves that minimize the fluctuation of the radial EMF were proposed in the literature [22–24] to reduce acoustic noise and torque ripple. These methods not only improve the radial EMF fluctuation characteristics and reduce the vibration, but also minimize the iron loss. Tavakoli et al. [25] adopted a new power converter to reduce unbalance EMF and torque ripple of the SRM by the winding current control. Gundogmus et al. [26] presented a multiobjective optimization algorithm for current distribution, which simultaneously reduce torque ripple and radial EMF fluctuation.

To control the radial EMF more simply and effectively, the control strategies of the turn-on and turn-off angle were investigated. Zhong et al. [27] provided an analytical method to derive the main current and radial vibration order caused resonance and analyzed the effects of different switching angles on current and radial vibration. They found that the advancement of turn-on angle and the delay of the turn-off angle reduced the third-order and sixth-order harmonics of the radial vibration. Zhang et al. [28] proposed a control method of variable turn-off angle based on the transfer function between the radial EMF and acceleration, which is better than traditional PWM method to reduce vibration. Guo et al. [29] deduced the third-order current harmonic, which caused the sixth-order radial vibration harmonic in three-phase SRM. It is found that the third-order current harmonic and the sixth-order radial vibration harmonic will decrease with the increase of the advancement of turn-on angle and the delay of the turn-off angle.

Though many attributions to suppress radial EMF for SRMs have been made in the above studies, the researches on structural optimization and control strategy for SRM are insufficient. For example, in the aspect of structure optimization, the main focuses are on improving strength of stator structure without considering the reduction of radial EMF; in the aspect of control strategy, most control methods are complex and not easy to be applied in practice.

In the presented investigation, considering the torque loss, an improved SRM model with DAS was proposed and the effects of initial rotor position, the turn-on and turn-off angles on radial EMF, and output torque were investigated to reduce the radial EMF and suppress vibration. We first established the simulation model of different SRMs. Then, we explored the effects of the parameters on the magnetic density distribution and radial EMF of the improved SRM and decided the optimal parameter set.

2. SRM Mathematical Model

2.1. SRM Simulation Model. The investigated model is a three-phase 12/8 SRM with four stator poles and four coils per phase, and the schematic of the model can be seen from Figure 1. The coils for phase A are denoted by A1, A2, A3, and A4, and other phases are denoted in a similar way. The basic parameters of the SRM are listed in Table 1 [30].

Figures 1(a)–1(d) illustrate four different types SRMs, which are without auxiliary slots (conventional SRM), stator with auxiliary slots, rotor with auxiliary slots, and double auxiliary slots (DAS), respectively. When the rotor pole is in the mid-way position, the rotor position θ is defined as 0°, and when the rotor pole in the aligned position, $\theta = 11.25^{\circ}$ obtained by the following equation:

$$\theta = \frac{360^{0} \times N_p}{N_r \times N_s}, \tag{1}$$

where N_p, N_r, and N_s are the number of phase, the number of rotor pole, and the number of stator pole, respectively.

To simplify the analysis, the mutual inductance is neglected because it is far less than self-inductance.

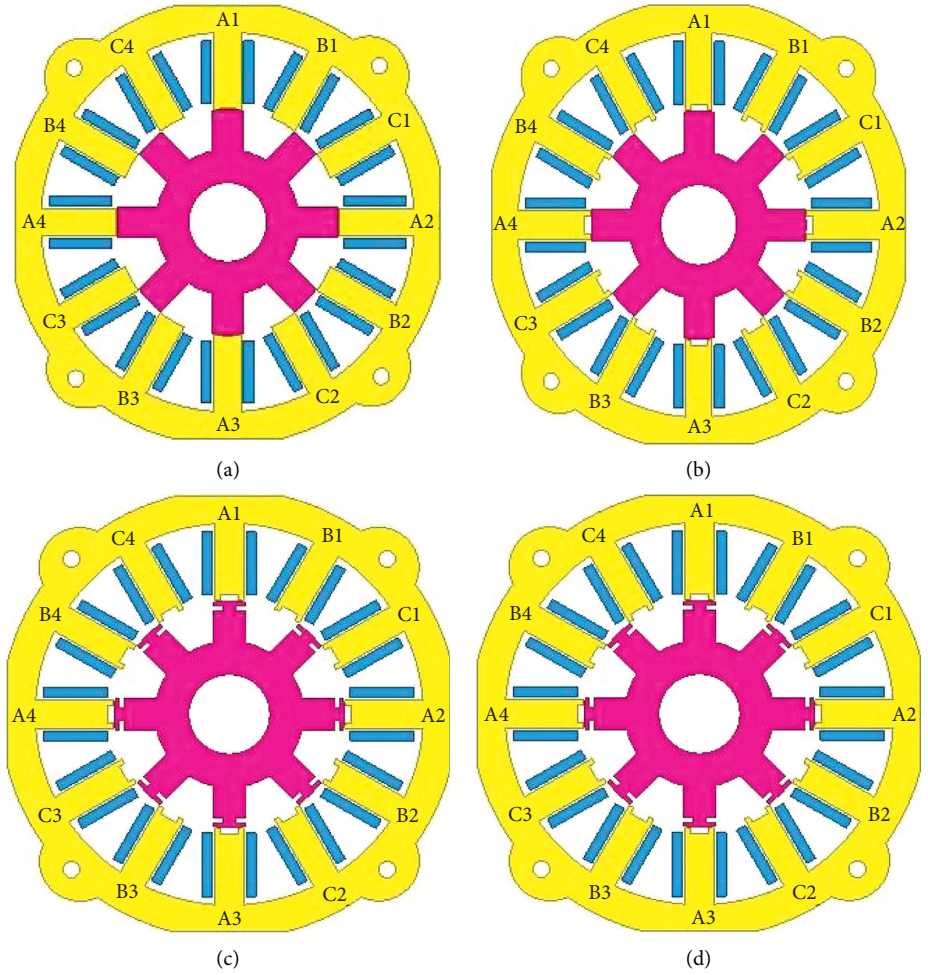

Figure 1: Schematic of the SRM. (a) No auxiliary slot. (b) Stator with auxiliary slot. (c) Rotor with auxiliary slot. (d) Double auxiliary slot.

Table 1: Basic parameters of SRM.

Specification	Value
Rated power	3 kW
Rated voltage	310 V
Stator outer diameter	135 mm
Stator inter diameter	68.8 mm
Rotor outer diameter	68 mm
Rotor inter diameter	24 mm
Core length	80 mm
Stator poles	12
Rotor poles	8

2.2. Electromechanical Equations. Firstly, the magnetic coenergy $W(i,\theta)$ at any position θ and current i is defined as follows:

$$W(i,\theta) = \int_0^i \psi(i,\theta)\mathrm{d}i, \tag{2}$$

where $\psi(i,\theta)i$ is a magnetic linkage. The magnetic coenergy is equal to the mechanical energy; that is, $W(i,\theta) = W_m$. At a constant current, the instantaneous torque T and the radial EMF F_r generated by the SRM can be calculated according to the following equations:

$$T = \frac{\partial W(i,\theta)}{\partial\theta}\Big|i = \text{const}, \tag{3}$$

$$F_r = \frac{\partial W(i,\theta)}{\partial l_g}\Big|i = \text{const}, \tag{4}$$

where l_g is the air gap.

Since $\psi(i,\theta)$ is determined by the inductance $L(i,\theta)$ and current i, the $L(i,\theta)$ value, i value, and mechanical output of the machine are calculated by the electromagnetic, voltage, and torque equations.

2.3. Electromagnetic Equations. The Fourier series method was proposed to calculate $L(i,\theta)$. Since the first three terms of Fourier expansion are sufficient to describe the dynamic characteristics of SRM, $L(i,\theta)$ can be expressed as follows:

$$L(i,\theta) = L_0(i) + L_1(i)\cos(N_r\theta + \pi) + L_2(i)\cos(2N_r\theta + 2\pi), \tag{5}$$

where $L_0(i)$, $L_1(i)$ and can be expressed as

$$L_0(i) = \frac{1}{2}\left[\frac{1}{2}(L_a(i) + L_u) + L_m(i)\right], \tag{6}$$

$$L_1(i) = \frac{1}{2}(L_a(i) - L_u), \tag{7}$$

$$L_2(i) = \frac{1}{2}\left[\frac{1}{2}(L_a(i) + L_u) - L_m(i)\right], \tag{8}$$

where L_a is the inductance in the aligned position, L_u denotes the inductance in the unaligned position, and L_m denotes the inductance in the mid-way position. Since no unsaturation appears in the unaligned position, L_u can be treated as a constant and it is independent of the current. With the data obtained from experiments or FEA models, both $L_a(i)$ and $L_m(i)$ can be fitted by polynomials with coefficients of a_n and b_n, respectively, and N is the number of Fourier terms.

$$\begin{aligned} L_a(i) &= \sum_{n=0}^{N} a_n i^n, \\ L_m(i) &= \sum_{n=0}^{N} b_n i^n. \end{aligned} \tag{9}$$

By combining equations (5)–(9), the inductance of the phase k ($k = A, B, C$) with current i_k can be expressed as

$$\begin{aligned} L(i_k,\theta) = {} & \frac{1}{2}L_a(i_k)\left[\cos^2(N_r\theta) - \cos(N_r\theta)\right] \\ & + \frac{1}{2}L_u\left[\cos^2(N_r\theta) + \cos(N_r\theta)\right] + \sin^2(N_r\theta)L_m(i_k). \end{aligned} \tag{10}$$

The relationship between magnetic linkage and inductance can be expressed as

$$\psi(i_k,\theta) = \int_0^{i_k} L(i_k,\theta)\mathrm{d}i_k. \tag{11}$$

2.4. Mechanical Equations. After obtaining the magnetic linkage $\psi(i_k,\theta)$, the torque per phase of SRM can be calculated by

$$T_k = \int_0^{i_k} \frac{\partial\psi(i_k,\theta)}{\partial\theta}\mathrm{d}i_k. \tag{12}$$

Therefore, the total SRM torque is defined as

$$T_{\text{overall}} = \sum_{K=1}^{3} T_K. \tag{13}$$

Using a procedure similar to the torque calculation and by neglecting the leakage flux, the radial EMF of the SRM can be calculated as

$$F_{rk} = \frac{T_{k\delta}}{l_o}, \tag{14}$$

where l_o is the overlap angle between the stator and the rotor.

2.5. Circuit Equations. The relationship between the phase flux and the k-phase current follow Faraday's law:

$$U_k = R_k i_k + \frac{\mathrm{d}\psi_k}{\mathrm{d}t}, \tag{15}$$

where $\psi(i_k,\theta)$ is expressed in equation (10), from which it can be seen that $\psi(i,\theta)$ is a function of i and θ, so (14) can be rewritten as

$$U_k = R_k i_k + L_k(i_k,\theta)\frac{\mathrm{d}i_k}{\mathrm{d}t} + w\frac{\partial\psi_k}{\partial\theta}, \tag{16}$$

where w is rotor angular velocity, the phase current i_k can be expressed as

$$i_k = \int \frac{U_k - R_k i_k - w(\partial\psi_k/\partial\theta)}{L_k(i_k,\theta)}\mathrm{d}t. \tag{17}$$

3. Results and Discussion

To simplify the magnetic field analysis, a two-dimensional magnetic field calculation was carried out for the SRMs with different structures in Figure 1 using commercial codes of ANSOFT Maxwell. First, the magnetic density distribution and radial EMF of the four different types of SRMs were compared in Section 3.1. Then, the effect of the parameters including initial rotor position and the turn-on and turn-off angle on radial EMF of the improved SRM was explored in Section 3.2. Thereafter, the optimal parameter set for the SRM with DAS was decided by orthogonal experimental design and comparison of the values of the radial EMF and torque in Section 3.3.

3.1. Radial EMF Comparison. The distribution contours of magnetic induction intensity obtained were shown in Figures 2(a)–2(d). When a single-phase was energized, the rotor teeth begin to rotate along the direction of the least magnetoresistance. In the process, the magnetic induction intensity is greatest when the stator and rotor are just aligned. It can be seen from Figures 2(a) to 2(d) that the number of magnetic field line going through the rotor teeth from the stator teeth is 9, 8, 9, and 8, respectively. As for the direction of the magnetic line of force, in Figure 2(a) and 2(b), the magnetic line of force distribute in vertical direction, while in Figures 2(c) and 2(d), those distribute in horizontal direction. The results indicate that the stator with auxiliary slots is helpful to reduce the number of magnetic line of force, and the rotor with auxiliary slots helps to change the direction of the magnetic line of force, which contributes to reducing the radial component of the electromagnetic force. The SRM with DAS combines the advantages of the stator and rotor with auxiliary slots.

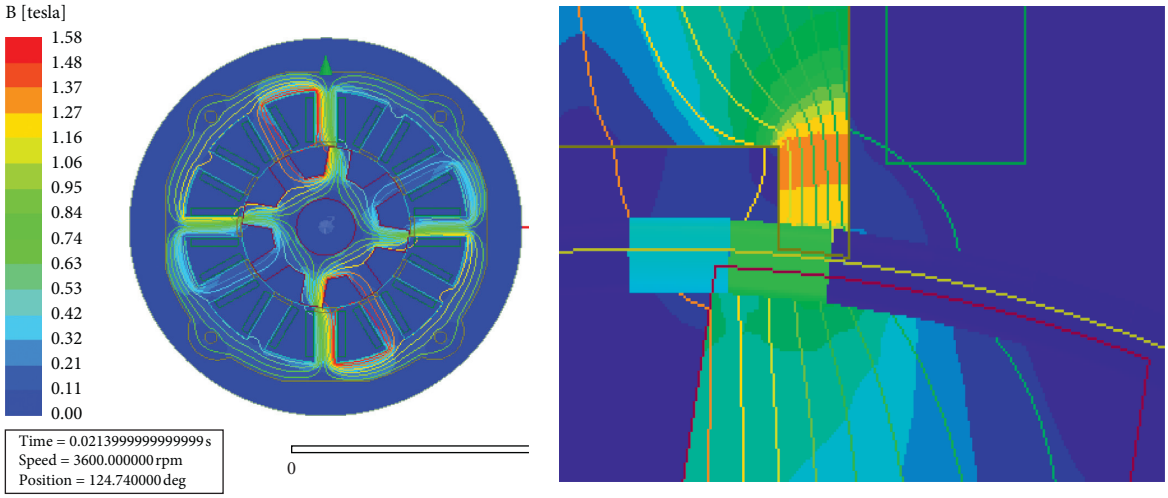

(a)

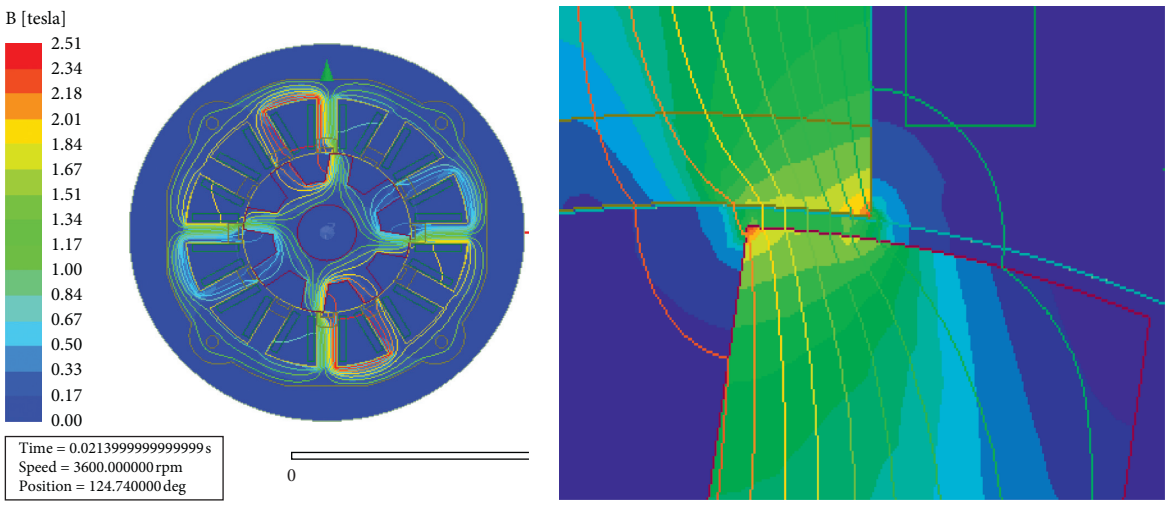

(b)

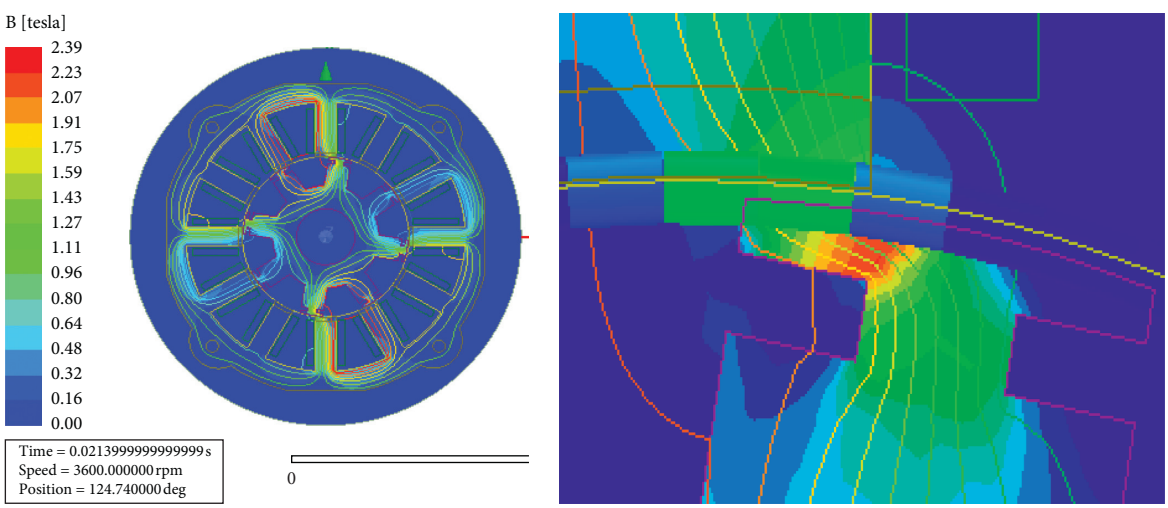

(c)

Figure 2: Continued.

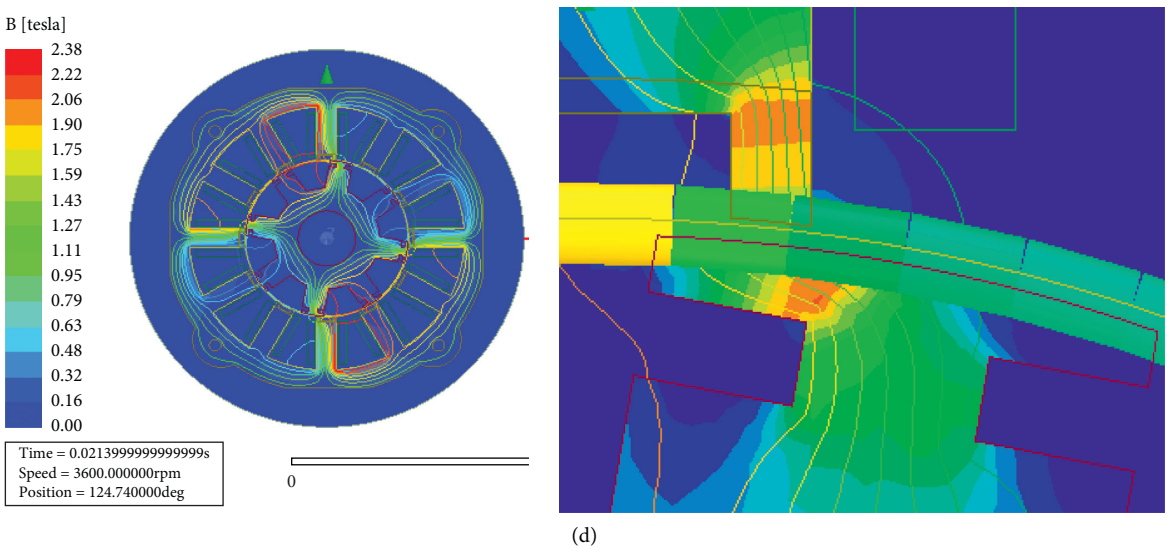

(d)

Figure 2: The distribution contours of magnetic induction and magnetic flied line. (a) No auxiliary slots. (b) Stator with auxiliary slots. (c) Rotor with auxiliary slots. (d) Double auxiliary slots.

A magnetic density distribution along the circumferential direction within 360° is plotted based on the magnetic density distribution in the air gap of Figures 2(a) to 2(d). It can be observed from Figure 3 that, when the phase A is on, the magnetic flux density of phase A is greater than that of phases B and C, because the number of magnetic lines of force passing through the coils of phases B and C is less than that of phase A.

The uniform magnetic density at each moment causes the different magnitude of the radial EMF. According to the maximum radial EMF at different moments, the radial EMF profile is plotted in Figure 4. It can be seen that the average radial EMF magnitudes of the four different SRMs within 10 ms are about 443 N, 404 N, 399 N, and 386 N, respectively. The radial EMF magnitude of the conventional SRM is greater than that with auxiliary slots. Meanwhile, the radial EMF magnitudes with the single auxiliary slots are greater than those with the DAS. The results indicate that the auxiliary slot structure, especially, the DAS structure, has a remarkable effect on reducing the radial EMF.

3.2. Performance Analysis of SRM with DAS. At the rated speed of 3600 r/min and rated power of 3 kW, the SRM with DAS was simulated at different initial rotor position θ, turn-on angle φ, and turn-off angle β. The radial EMF and maximum electromagnetic torque profiles are plotted in Figures 5 and 6, respectively.

3.2.1. Average Radial EMF. It can be seen from Figure 5 that the effects of turn-on angle φ and turn-off angle β on the average radial EMF F_{r_avg} when the rotor is at different θ. In Figure 5(a), when β is 15°, the value of F_{r_avg} takes 86 N at $\varphi = 0°$. In contrast, the values of F_{r_avg} at $\varphi = -1°$ and $\varphi = -2°$ are increased by 41 N and 64 N, respectively. In Figures 5(b) and 5(c), taking the same set, the values of F_{r_avg} at $\varphi = -1°$ and $\varphi = -2°$ are increased by 43 N, 64 N and 107 N, 135 N, respectively. The same trends occur when β takes 13°, 18°, and 19°. It can be known from the above analysis that the average radial EMF increases with the advancement of turn-on angle and delay of the turn-off angle.

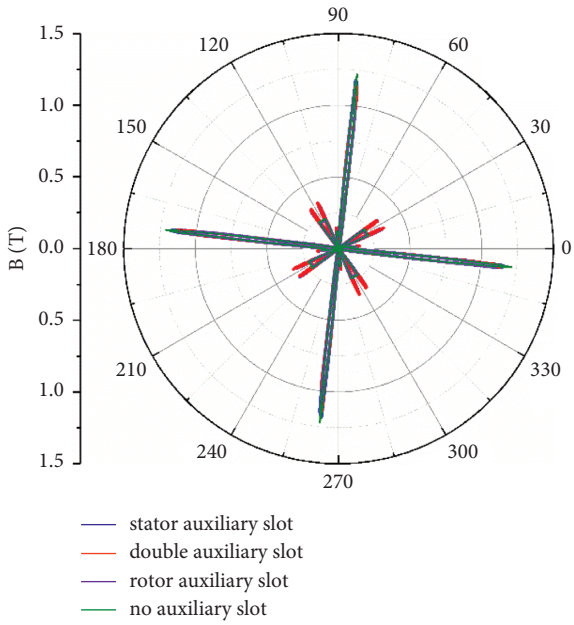

Figure 3: Distribution of flux density in the air gap.

As it can be seen in Figures 5(a)–5(c), the average radial EMFs increase with the increase of the initial rotor position angle θ when the turn-on angle and the turn-off angle are constant. For example, at $\varphi = 0°$ and $\beta = 13°$, taking three initial rotor positions angle 7.5°, 15°, and 22.5°, the values of F_{r_avg} are 48 N, 114 N, and 214 N, respectively. Based on the above analysis, there is a significant upward trend of the average radial EMF with the advancement of the turn-on angle and increase of initial rotor position or the delay of the turn-off angle.

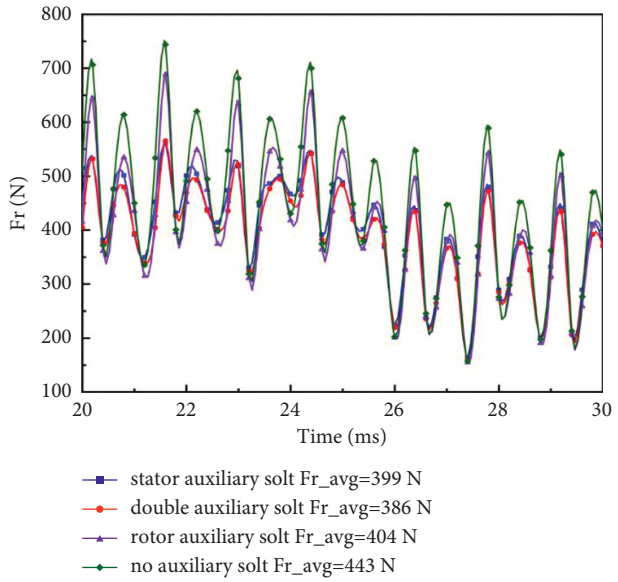

Figure 4: Radial EMF versus time for difference SRM models.

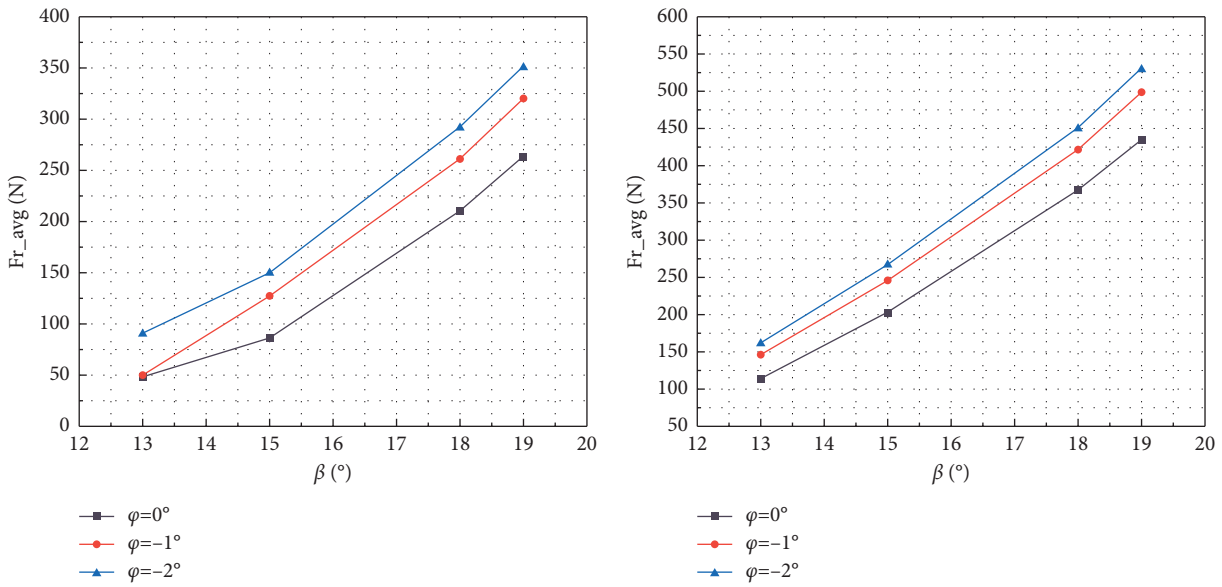

Figure 5: Continued.

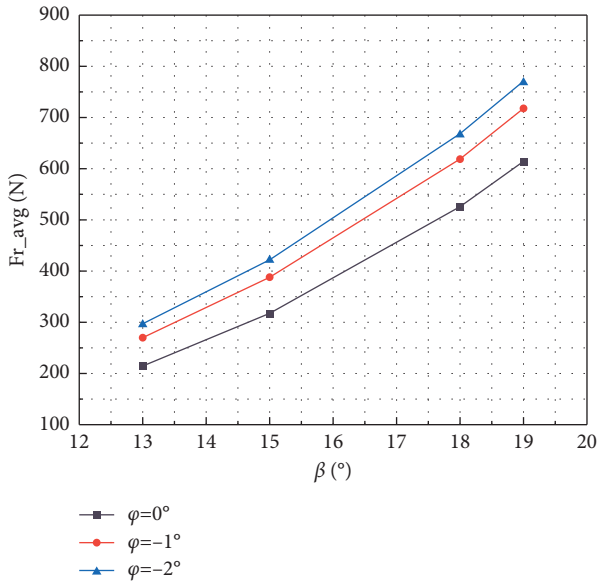

(c)

Figure 5: The average radial EMF versus turn-off angle for different turn-on angle. (a) $\theta = 7.5^{\circ}$. (b) $\theta = 15^{\circ}$. (c) $\theta = 22.5^{\circ}$.

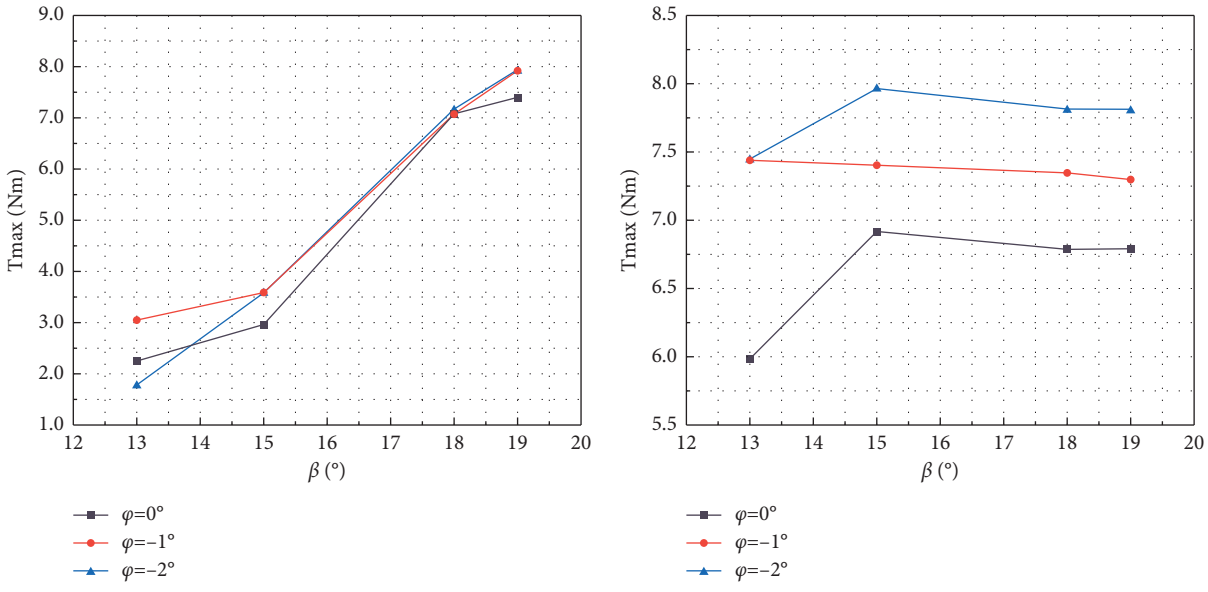

(a) (b)

Figure 6: Continued.

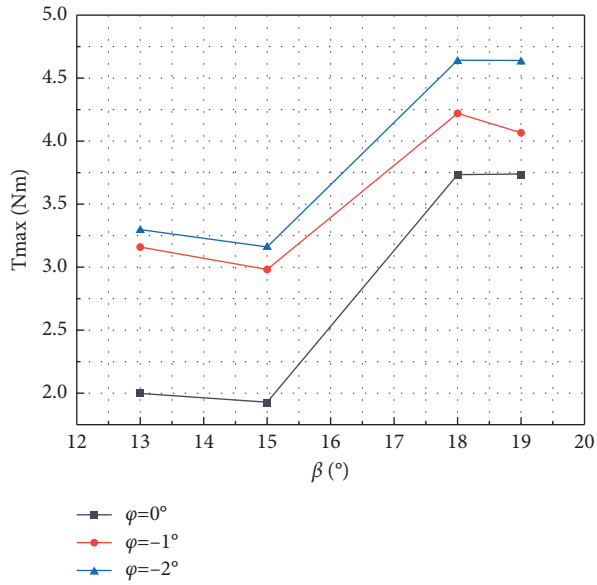

(c)

Figure 6: The maximum electromagnetic torque versus turn-off angle for different turn-on angle. (a) θ = 7.5°. (b) θ = 15°. (c) θ = 22.5°.

3.2.2. Maximum Electromagnetic Torque. In Figures 6(a) and 6(c), the maximum electromagnetic torque T_{max} increases with the decrease of the turn-off angle, especially in the range of 15° to 18°. The maximum electromagnetic torque at $\varphi = 0°$ increases from 2.97 Nm to 7.09 Nm in Figure 6(a). However, at θ of 15°, the curves of maximum electromagnetic torque are flat without significant fluctuation in Figure 6(b), particularly, when the turn-off angle is greater than 15°. The maximum electromagnetic torque at φ of −1° reduces only by 0.06 Nm when the turn-off angle varies from 15° to 18°.

In addition, the maximum electromagnetic torques at the three initial rotor positions totally increase with the increase of the turn-on angle (except $\beta = 13°$ in the Figure 6(a)). In Figure 6(c), when β takes 18° and φ are 0°, −1°, and −2°, the values of T_{max} are 3.73 Nm, 4.21 Nm, and 4.64 Nm, respectively. In contrast, it can be seen from the Figures 6(a)–6(c) that when φ and β are a constant, the maximum electromagnetic torque increases first and then decreases with the increase of θ (except $\beta = 19°$), and the maximum electromagnetic torques in Figure 6(b) are overall greater than that in Figures 6(a) and 6(c).

3.3. Optimization on Vibration

3.3.1. Experiment Design. Based on the factors and levels listed in Table 2, an L9 (3^4) orthogonal experimental table was designed as Table 3. The average radial EMF F_{r_avg} was used as the indicator of the radial EMF. The optimal set of factors was determined by analysis of variance, and the variance analysis table is obtained as Table 4.

The order of the k_{ij} ($i = 2, 3$; $j = 1, 2, 3$) can be seen from Table 3 and expressed as follows:

Table 2: Experimental factors and levels.

	φ (°)	β (°)	θ (°)
Level 1	0	13	7.5
Level 2	−1	15	15
Level 3	−2	18	22.5

Table 3: Orthogonal experimental table.

	φ (°)	β (°)	θ (°)	Fr_avg (N)
1	1	1	1	48
2	1	2	2	203
3	1	3	3	526
4	2	1	2	146
5	2	2	3	338
6	2	3	1	261
7	3	1	3	296
8	3	2	1	150
9	3	3	2	452
K_{j1}	777.2	490.2	459	
K_{j2}	745.9	691.5	801.4	
K_{j3}	897.2	1238.6	1159	

$$K_{23} > K_{22} > K_{21},$$
$$K_{33} > K_{32} > K_{31}. \quad (18)$$

Based on Table 4, the effects of factor β and θ on F_{r_avg} are significant. To minimize average radial EMF, β_1 and θ_1 were chosen as optimal factors. In addition, the effect of the turn-on angle on the radial EMF is not significant, so φ_1 was chosen. Finally, the optimal set for the minimum average radial EMF is $\phi_1\beta_1\theta_1$.

Table 4: Variance analysis table of average radial electromagnetic force.

Source of variance	Degree of freedom	Sum of square	Mean square error	F value	Significance
φ (°)	2	4252	2126	3.8	Not obvious
β (°)	2	99993	49997	88	Obvious
θ (°)	2	81891	40945	72	Obvious
Error	2	1132	566	—	—
Sum	8	187268	—	—	—

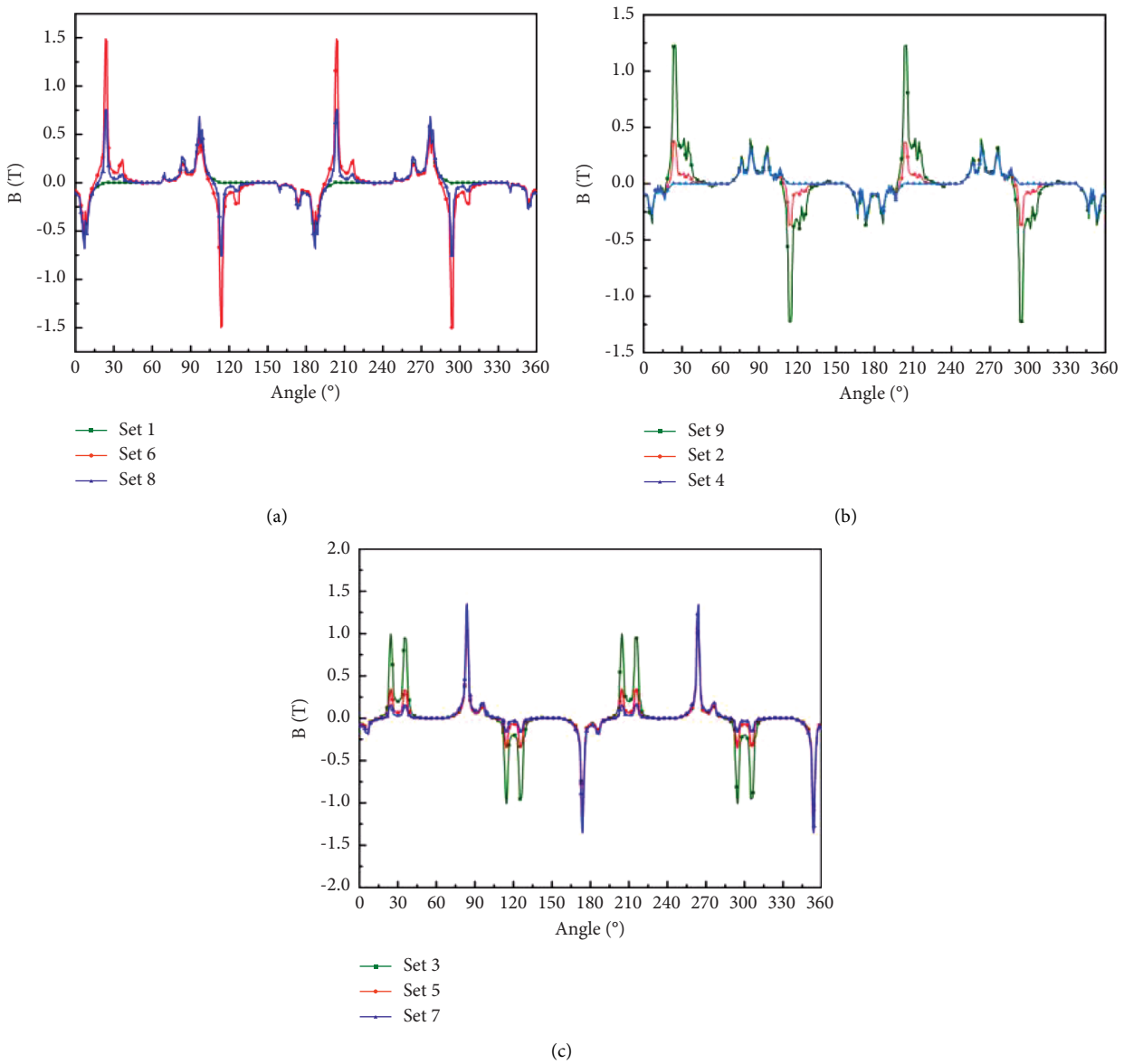

Figure 7: Radial magnetic density versus initial position for different parameter sets. (a) $\theta = 7.5^{\circ}$. (b) $\theta = 15^{\circ}$. (c) $\theta = 22.5^{\circ}$.

3.3.2. Radial Magnetic Density. The radial magnetic density profiles are plotted in Figure 7. It can be observed that when the rotor is located at different initial positions, the different moments of turn-on and turn-off significantly affect the radial magnetic density. The increase of radial magnetic density is mainly because two adjacent magnetic poles will work at the same time with the advancement of the turn-on angle or the delay of the turn-off angle.

To reduce of radial magnetic density, there are different optimal sets (i.e., sets 1, 4, and 5). Based on the three optimal sets, the radial magnetic density profiles are plotted in Figure 8. The radial magnetic density in the air gap at the optimal set 4 is the smallest. Based on the profiles in Figure 8, the FFT decomposition was conducted. The FFT diagram of radial magnetic density at the optimal sets is plotted in Figure 9. It can be seen that the harmonic magnitude is

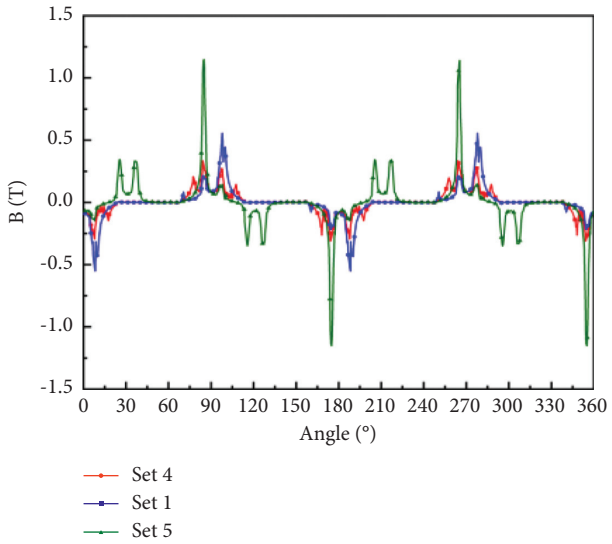

Figure 8: Radial magnetic density versus initial position for the optimal parameter sets.

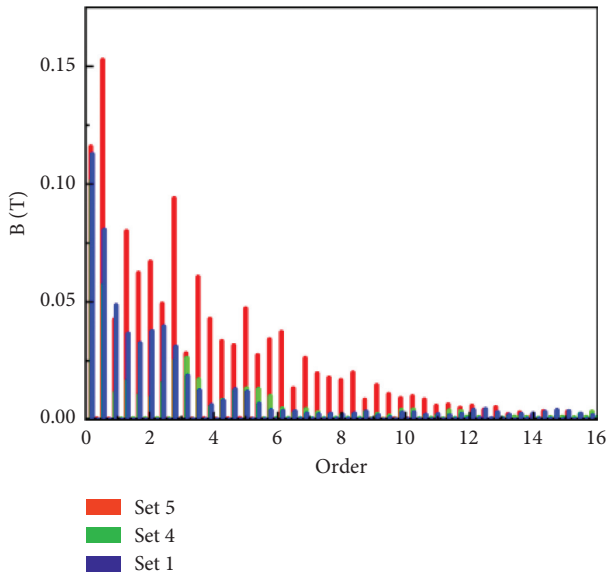

Figure 9: The FFT diagram of radial magnetic density at the optimal parameter sets.

smaller at the set 4 than that at other two sets, and the vibration magnitude is smallest.

3.3.3. Radial EMF. In can been seen from Figure 10 that the effect of each parameter set on the radial EMF is significantly difference. For example, in Figure 10(a), the magnitude at set 1 is significantly smaller than that at the other two sets and the average radial EMF is only 48 N at set 1, which is far smaller than 261 N and 150 N at sets 6 and 8. The cause is the shortest conduction width in set 1 among the three sets, and this result is consistent with the previous discussion in 3.2.1. The same trends are observed in Figures 10(b) and 10(c), but the magnitudes of average radial EMF are different. For example, in Figures 10(a)–10(c), the minimum magnitudes of average radial EMF are 48 N, 146 N, and 296 N at optimal sets 1, 4, and 7, respectively. At the condition of these three optimal sets, the radial EMF profiles are plotted in Figure 11. It can be seen that the radial EMF acting on the stator is the smallest at set 1. The results indicate that the radial EMF can be further weakened to suppress the machine vibration using the optimal θ, φ, and β.

The advancement of turn-on angle or the delay of turn-off angle or the increase of the initial rotor position affects not only the radial EMF of the SRM, but also the electromagnetic torque. It can be observed from Figure 12 that the electromagnetic torque undergoes different changes process with the time increase using three optimal sets. For example, the torque magnitude at set 1 fluctuated with remarkable positive and negative alternation. The maximum torque is 2.26 Nm, which is smaller than the maximum torques 7.44 Nm and 3.3 Nm at sets 4 and 7, respectively. Meanwhile,

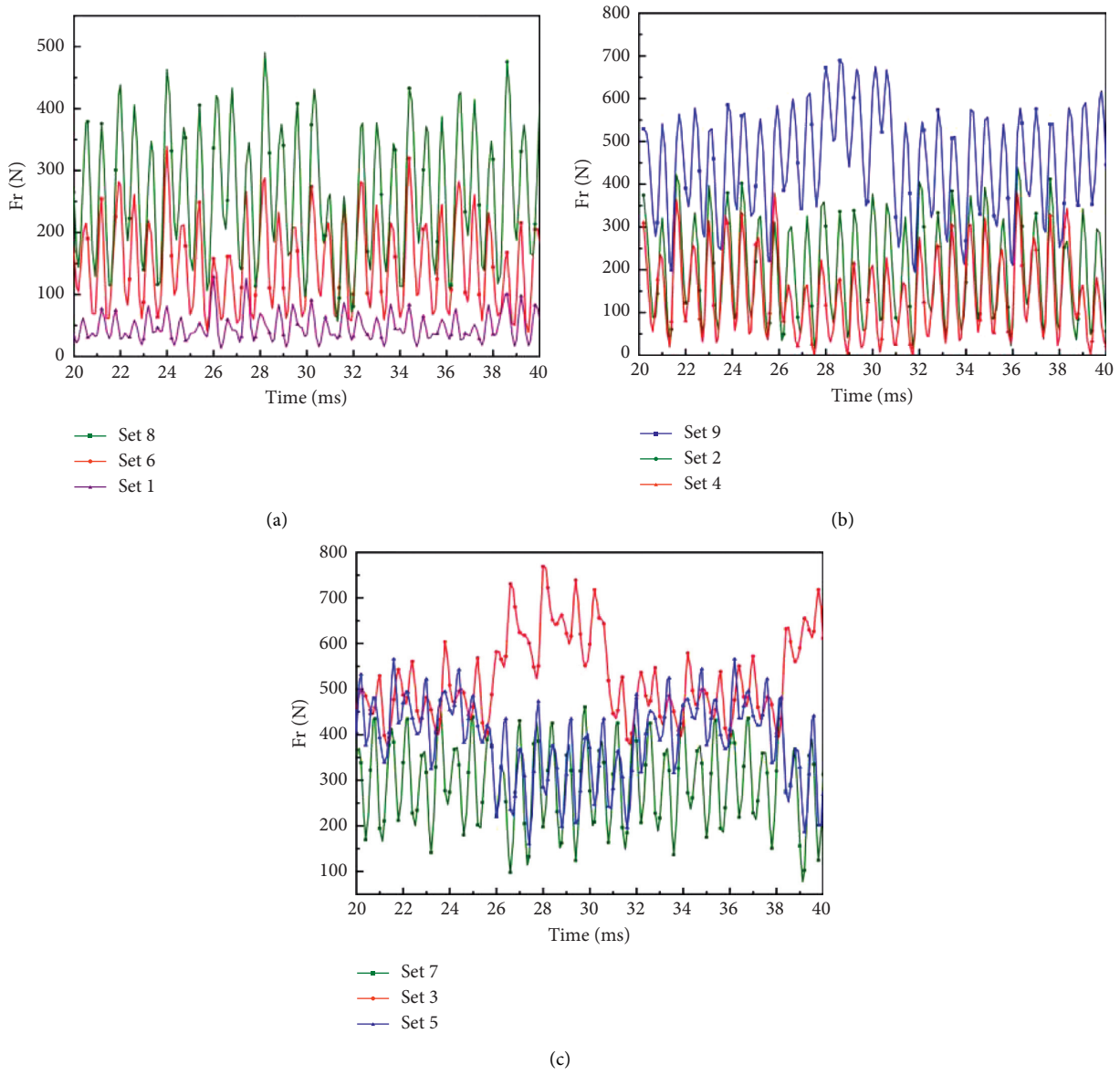

Figure 10: Radial EMF versus time for different φ, β sets. (a) $\theta = 7.5^{\circ}$. (b) $\theta = 15^{\circ}$. (c) $\theta = 22.5^{\circ}$.

the average torques are 1.58 Nm and 1.36 Nm at sets 4 and 7, respectively. In contrast to the conventional SRM, the torque at set 4 is closest to the output torque 1.83 Nm. Though the reduction of radial EMF is significantly beneficial for the suppression of SRM vibration, the magnitude of the torque needs to be considered comprehensively. In this case, the average radial EMF 48 N at set 1 is the smallest, but the value of the torque is also smallest and fluctuates wildly in positive and negative directions.

The reason for the fluctuation of torque is mainly because the turn-off angle is 13° in set 1. When the excitation poles were cut off, the magnetic poles of the rotor and stator have not been completely aligned, and the adjacent magnetic poles of stator have not been energized. The rotor will rotate due to inertia without any other applied force. At the same time, the counterelectromotive force will apply the force on the rotor in the opposite direction, which results in the torque in the negative direction. When the adjacent poles of the stator are energized, a positive force is applied to the rotor to produce a positive torque.

In contrast to sets 1 and 7, set 4 is a compromise, at which the average radial EMF of 146 N is greater than 48 N at set 1, but it is smaller than 296 N at set 7. The torque is higher at set 4 than that at the other two sets and without positive and negative alternation. At the same time, the harmonics of radial magnetic density is lowest at set 4, which minimizes the SRM vibration. Based on the above analysis, the optimal parameter set 4 is determined.

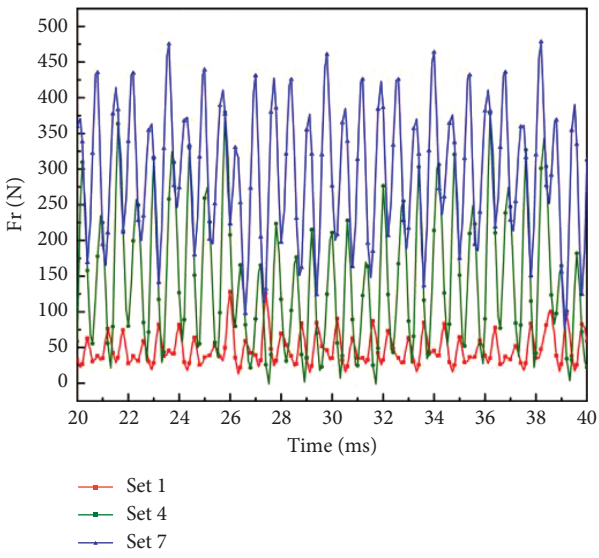

Figure 11: REF versus time for optimal φ, β sets.

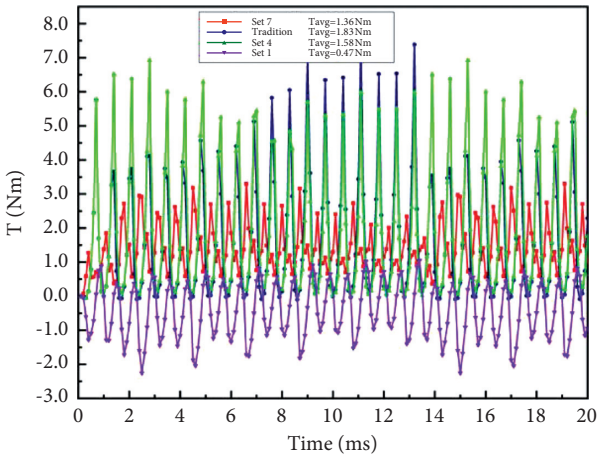

Figure 12: Torque versus time for optimal φ, β sets.

4. Conclusions

To enhance the vibration performance of SRM, an innovative SRM with DAS was proposed. The effects of the initial rotor position and turn-on and turn-off angles on the radial EMF and torque were investigated. The conclusions are as follows:

(1) Compared with conventional SRM, the SRM with DAS has obvious advantages to reduce the radial EMF ripple and suppress the vibration.

(2) The parameter sets of initial rotor position and turn-on and turn-off angles have an important effect on radial EMF ripple and torque, which will increase significantly with the advancement of the turn-on angle or the delay of the turn-off angle.

(3) For the improved SRM with DAS, the radial EMF is reduced to a lower level without obvious loss of torque at turn-on angle of −1°, turn-off angle of 13°, and rotor position of 15°.

Data Availability

The data supporting the conclusion of the article are shown in the relevant figures and tables provided.

Conflicts of Interest

The authors declare that they have no potential conflicts of interest with respect to the research, authorship, and/or publication of this article.

Acknowledgments

The present work was supported by the Scientific and Technological Research Program of Chongqing Science and Technology Bureau (Grants nos. cstc2016jcyjA0424 and cstc2019jcyj-msxmX0761) and the Scientific and Technological Research Program of Chongqing Municipal Education Commission (Grant no. KJQN201800731).

References

[1] X. D. Xue, K. W. E. Cheng, T. W. Ng, and N. C. Cheung, "Multi-objective optimization design of in-wheel switched reluctance motors in electric vehicles," *IEEE Transactions on Industrial Electronics*, vol. 57, no. 9, pp. 2980–2987, 2010.

[2] J. Ye, B. Bilgin, and A. Emadi, "An extended-speed low-ripple torque control of switched reluctance motor drives," *IEEE Transactions on Power Electronics*, vol. 30, no. 3, pp. 1457–1470, 2015.

[3] Y. Qin, C. He, X. Shao, H. Du, C. Xiang, and M. Dong, "Vibration mitigation for in-wheel switched reluctance motor driven electric vehicle with dynamic vibration absorbing structures," *Journal of Sound and Vibration*, vol. 419, pp. 249–267, 2018.

[4] X. Shao, F. Naghdy, H. Du, and Y. Qin, "Coupling effect between road excitation and an in-wheel switched reluctance motor on vehicle ride comfort and active suspension control," *Journal of Sound and Vibration*, vol. 443, pp. 683–702, 2019.

[5] D. Marcsa and M. Kuczmann, "Design and control for torque ripple reduction of a 3-phase switched reluctance motor," *Computers & Mathematics with Applications*, vol. 74, no. 1, pp. 89–95, 2017.

[6] A. Rezig, W. Boudendouna, A. Djerdir, and A. N'Diaye, "Investigation of optimal control for vibration and noise reduction in-wheel switched reluctance motor used in electric vehicle," *Mathematics and Computers in Simulation*, vol. 167, pp. 267–280, 2020.

[7] T. Kotegawa and I. Miki, "Stator structure for reducing noise in switched reluctance motor," in *Proceedings of the 2013 15th European Conference on Power Electronics and Applications (EPE)*, Lille, France, October 2013.

[8] G. Davarpanah and J. Faiz, "A novel structure of switched reluctance machine with higher mean torque and lower torque ripple," *IEEE Transactions on Energy Conversion*, vol. 35, no. 4, pp. 1859–1867, 2020.

[9] A. H. Isfahani and B. Fahimi, "Comparison of mechanical vibration between a double-stator switched reluctance machine and a conventional switched reluctance machine," *IEEE Transactions on Magnetics*, vol. 50, no. 2, pp. 293–296, 2014.

[10] T. D. Gupta, K. Chaudhary, R. M. Elavarasan, R. K. Saket, I. Khan, and E. Hossain, "Design modification in single-tooth

winding double-stator switched reluctance motor for torque ripple mitigation," *IEEE Access*, vol. 9, pp. 19078–19096, 2021.

[11] Z. Yu, K. Cheng, N. C. Cheung, and J. Pan, "Deformation and noise mitigation for the linear switched reluctance motor with skewed teeth structure," *IEEE Transactions on Magnetics*, vol. 50, no. 11, pp. 1–4, 2014.

[12] G. Li, J. Ojeda, S. Hlioui, E. Hoang, M. Lecrivain, and M. Gabsi, "Modification in rotor Pole geometry of mutually coupled switched reluctance machine for torque ripple mitigating," *IEEE Transactions on Magnetics*, vol. 48, no. 6, pp. 2025–2034, 2012.

[13] H. Zhang, J. Zhang, and R. Gao, "Radial force reduction for switched reluctance motor with skewed slot structure based on FEM," *Journal of Scientific and Industrial Research*, vol. 69, no. 8, pp. 594–599, 2010.

[14] H.-Y. Yang, Y.-C. Lim, and H.-C. Kim, "Acoustic noise/vibration reduction of a single-phase SRM using skewed stator and rotor," *IEEE Transactions on Industrial Electronics*, vol. 60, no. 10, pp. 4292–4300, 2013.

[15] C. Gan, J. Wu, M. Shen, S. Yang, Y. Hu, and W. Cao, "Investigation of skewing effects on the vibration reduction of three-phase switched reluctance motors," *IEEE Transactions on Magnetics*, vol. 51, no. 9, pp. 1–9, 2015.

[16] A. Sakuma, M. Kadowaki, H. Ukigai, I. Miki, T. Okamoto, and T. Segawa, "Stator structure for noise reduction of switched reluctance motor," in *Proceedings of the 2012 15th International Conference on Electrical Machines and Systems (ICEMS)*, Sapporo, Japan, January 2013.

[17] M. Elamin, Y. Yasa, Y. Sozer, J. Kutz, J. Tylenda, and R. L. Wright, "Effects of windows in stator and rotor poles of switched reluctance motors in reducing noise and vibration," in *Proceedings of the 2017 IEEE International Electric Machines and Drives Conference (IEMDC)*, Miami, FL, USA, August 2017.

[18] K. Takayama and I. Miki, "Design of switched reluctance motor to reduce acoustic noise," in *Proceedings of the International Symposium on Power Electronics*, IEEE, Capri, Italy, August 2016.

[19] M. A. J. Kondelaji and M. Mirsalim, "Segmented-rotor modular switched reluctance motor with high torque and low torque ripple," *IEEE Transactions on Transportation Electrification*, vol. 6, no. 1, pp. 62–72, 2020.

[20] A. Tanabe and K. Akatsu, "Vibration reduction method in SRM with a smoothing voltage commutation by PWM," in *Proceedings of the International Conference on Power Electronics & ECCE Asia*, pp. 600–604, IEEE, Seoul, Korea (South), July 2015.

[21] A. Malekipour, S. M. Saghaiannezhad, and A. Rashidi, "A method for vibration alleviation of SRM when demagnetization voltage is boosted," in *Proceedings of the International Power Electronics Drive Systems and Technologies Conference*, pp. 138–142, Shiraz, Iran, April 2019.

[22] M. Takiguchi, H. Sugimoto, N. Kurihara, and A. Chiba, "Acoustic noise and vibration reduction of SRM by elimination of third harmonic component in sum of radial forces," *IEEE Transactions on Energy Conversion*, vol. 30, no. 3, pp. 883–891, 2015.

[23] J. Furqani, M. Kawa, K. Kiyota, and A. Chiba, "Current waveform for noise reduction of a switched reluctance motor under magnetically saturated condition," *IEEE Transactions on Industry Applications*, vol. 54, no. 1, pp. 213–222, 2018.

[24] M. Kawa, K. Kiyota, J. Furqani, and A. Chiba, "Acoustic noise reduction of a high efficiency switched reluctance motor for hybrid electric vehicles with novel current waveform," *IEEE Transactions on Industry Applications*, vol. 55, no. 3, pp. 2519–2528, 2018.

[25] M. R. Tavakoli, H. Torkaman, F. Faradjizadeh, and E. Afjei, "Unbalanced magnetic force mitigation and torque ripple reduction in eccentric switched reluctance motors using flux leakages," *Electric Power Components and Systems*, vol. 43, no. 5, pp. 533–542, 2015.

[26] O. Gundogmus, L. Vadamodala, Y. Sezer, J. Kutz, J. Tylenda, and R. L. Wright, "Simultaneous torque and radial force ripple mitigation in DQ controlled switched reluctance machines," in *Proceedings of the 2019 IEEE International Electric Machines & Drives Conference (IEMDC)*, pp. 260–265, San Diego, CA, USA, August 2019.

[27] R. Zhong, X. Guo, M. Zhang, D. Ding, and W. Sun, "Influence of switch angles on second-order current harmonic and resonance in switched reluctance motors," *IET Electric Power Applications*, vol. 12, no. 9, pp. 1247–1255, 2018.

[28] M. Zhang, X. Mininger, I. Bahri, and C. Vlad, "Improvement of the variable turn-off angle control for SRM regarding vibration reduction," in *Proceedings of the 2017 IEEE International Electric Machines and Drives Conference (IEMDC)*, Miami, FL, USA, August 2017.

[29] X. Guo, R. Zhong, M. S. Zhang, D. Ding, and W. Sun, "Resonance reduction by optimal switch angle selection in switched reluctance motor," *IEEE Transactions on Industrial Electronics*, vol. 67, no. 3, pp. 1867–1877, 2019.

[30] J. Li and Y. Cho, "Dynamic reduction of unbalanced magnetic force and vibration in switched reluctance motor by the parallel paths in windings," *Mathematics and Computers in Simulation*, vol. 81, no. 2, pp. 407–419, 2010.